

Formation of wind-capture discs in Supergiant X-ray binaries

Consequences for Vela X-1 and Cygnus X-1

I. El Mellah¹, A. A. C. Sander², J. O. Sundqvist³, and R. Keppens¹

¹ Centre for mathematical Plasma Astrophysics, Department of Mathematics, KU Leuven, Celestijnenlaan 200B, B-3001 Leuven, Belgium

e-mail: ileyk.elmellah@kuleuven.be

² Institut für Physik und Astronomie, Universität Potsdam, Karl-Liebknecht-Str. 24/25, 14476 Potsdam, Germany

³ KU Leuven, Instituut voor Sterrenkunde, Celestijnenlaan 200D, B-3001 Leuven, Belgium

Received ...; accepted ...

ABSTRACT

Context. In Supergiant X-ray binaries (SgXB), a compact object captures a fraction of the intense wind from an O/B Sg companion star on a close orbit. Proxies exist to evaluate the efficiency of mass and angular momentum wind accretion but they depend so dramatically on the wind speed that within the theoretical and observational uncertainty ranges, they only bring loose constraints. Furthermore, they often bypass the impact of orbital and dissipative effects on the flow structure.

Aims. We study the wind dynamics and in particular, the angular momentum it gains and carries as it is accreted. We aim at evaluating the conditions of the formation of a disc-like structure around the accretor and the observational consequences for SgXB.

Methods. We use recent results on the wind launching mechanism to compute ballistic wind streamlines in the three-dimensional co-rotating frame of a binary system, accounting for the gravitational and radiative influence of the compact companion. Once it enters the Roche lobe of the accretor, we solve the hydrodynamics equations and evaluate the impact of different cooling prescriptions on the flow.

Results. A shocked region forms around the accretor as the flow is beamed. For wind speeds of the order of the orbital speed, the shock is highly asymmetric compared to the axisymmetric bow shock obtained for a purely planar homogeneous flow. Provided we enable cooling within the shocked region, the flow always circularizes for wind speeds low enough.

Conclusions. Although the donor star does not fill its Roche lobe, a realistic wind-launching representation can lead to a flow slow enough when it enters the Roche lobe of the accretor to be significantly beamed and bent by the orbital effects. The net angular momentum of the accreted flow is then sufficient to form, downstream the shock, a persistent disc-like structure whose properties depend on the cooling mechanism.

Key words. accretion, accretion discs – X-rays: binaries – stars: neutron, supergiants, winds, outflows – methods: numerical

1. Introduction

Most stars are found in multiple stellar systems, especially the high mass ones (Duchêne and Kraus 2013). Among them, a significant fraction will undergo a phase of mass transfer which can seriously alter their subsequent evolution. New observational insights on the long (Abbott et al. 2016) and short term (Grinberg et al. 2017) evolution of High Mass X-ray Binaries (HMXB) has aroused the compelling need for a more comprehensive description of mass transfer via wind accretion.

In Supergiant X-ray binaries (SgXB), a supergiant O/B donor star is orbited by a compact object, generally a neutron star (NS), embedded in the stellar wind (for a recent review, see Martínez-Núñez et al. 2017). O/B stars are known to lose mass at a rate up to several $10^{-6} M_{\odot} \text{yr}^{-1}$ through a wind whose launching mechanism was first determined by Lucy and Solomon (1970) and Castor et al. (1975) : the resonant line absorption of UV photons by partly ionized metal ions provides the outer layers of the star with a net outwards momentum. As the flow accelerates, it keeps tapping previously untouched Doppler-shifted photons and can reach terminal speeds up to $2,000 \text{km s}^{-1}$. It is the gravitational capture of a fraction of this abundant line-driven

wind by the compact companion which produces the X-ray luminosity we observe in SgXB, of the order of $10^{35-37} \text{erg s}^{-1}$.

Until now, the mass and angular momentum accretion rates pertaining wind accretion have been evaluated based on the Bondi-Hoyle-Lyttleton model (BHL, see Edgar 2004, for a review) : a planar supersonic flow is gravitationally deflected by the gravitational field of a point-mass and an overdense tail is formed in its wake. The mass accretion rate turned out to be extremely sensitive to the relative speed of the flow with respect to the accretor. In SgXB, the terminal wind speed is generally measured within $\sim 20\%$ but the accretor lies very close from the stellar surface, in a region where the wind is still accelerating and where orbital effects significantly alter the picture of a purely radial wind, only valid for an isolated star : the theoretical uncertainty on the magnitude and orientation of the wind velocity field within the orbital separation makes the sharp dependency of the BHL mass accretion rate even more crippling. Furthermore, the axisymmetry of the BHL problem has circumvented any discussion on the accretion of angular momentum. This assumption was first relaxed by Illarionov and Sunyaev (1975) and Shapiro and Lightman (1976) to assess the possibility of the formation of a wind-capture disc around compact accretors : they concluded that it was likelier for close binaries, where the star gets close to

fill its Roche lobe, but that it was, once again, highly dependent on the relative wind speed. Once we account for the inhomogeneities known to form in this type of winds (Sundqvist et al. 2017), any realistic SgXB X-ray accretion luminosity can be reproduced.

The archetype of classic SgXB is Vela X-1 where a NS is on a ~ 9 days eclipsing orbit around HD 77581, a B0.5 Ib Sg (Hiltner et al. 1972; Forman et al. 1973). The NS is deeply embedded in the intense stellar wind (associated to a mass loss rate of $\sim 1.3 \cdot 10^{-6} M_{\odot} \text{yr}^{-1}$ Gimenez-Garcia et al. 2016) with an orbital separation of approximately 1.8 stellar radii (Quaintrell et al. 2003). The most recent observations revealed a terminal wind speed lower than initially claimed, of the order of 600 to 700 km s^{-1} , consistent with numerical computation from first principles (Sander, Fürst, Kretschmar, Oskinova, Todt, Hainich, Shenar and Hamann 2017). These results suggest that orbital effects might dominate the dynamics between the stellar surface and the NS, and supply the wind with a significant amount of net angular momentum. It could lead to a complex accretion geometry, with a wind beamed enough towards the accretor that it could share some features with the Roche lobe overflow mass transfer (RLOF) at stake in Low Mass X-ray Binaries (LMXB). On the other hand, we know that Cygnus X-1, a SgXB hosting a black hole orbiting an O Sg which does not fill its Roche lobe (Orosz et al. 2011), the accretor is surrounded by an accretion disc, in spite of the mass transfer proceeding via the stellar wind. These two systems suggest that the wind-RLOF regime (first studied in the context of symbiotic binaries by Mohamed and Podsiadlowski 2007), could be the appropriate framework to understand the structure of the accretion flow, rather than the BHL or the RLOF geometries.

A fully consistent treatment of both the wind acceleration and its accretion by the compact object is required to avoid being left with the wind speed in the vicinity of the accretor as a convenient but unconstraining degree of freedom. Sander, Fürst, Kretschmar, Oskinova, Todt, Hainich, Shenar and Hamann (2017) computed the steady state wind stratification for a 1D radial non-local thermal equilibrium atmosphere of a star representative of the donor star in Vela X-1. They accounted for a plethora of chemical elements and ionization levels susceptible to absorb the stellar UV photons, and for the X-ray ionizing feedback from the accretor on the wind ionization state. In this paper, we intend to use this computed 1D line-driven acceleration to see how the 3D structure of the flow departs from a spherical wind once the orbital effects are added. Rather than being set based on an empirical fitting formula, the static wind velocity and density are mere consequences of the stellar and orbital properties. In section 2, we evaluate the systematic bending of the wind streamlines by the orbital effects, as the wind unfolds and reaches the Roche lobe of the accretor with a non-zero net angular momentum. Within the latter, we run 3D hydrodynamical simulations described in section 3 to capture the structure of the flow as it cools down downstream the shock and its capacity to form a disc-like structure. In section 4, the implications of such a component are discussed in the context of Vela X-1, and, to a lesser extent, of SgXB Cygnus X-1.

2. Orbital deviation of the wind

2.1. Model and numerical method

Sophisticated models and simulations of the launching of line-driven winds show that they become supersonic shortly above the stellar photosphere. It motivates a ballistic treatment of the

wind bulk motion at the orbital scale similar to what was done in El Mellah and Casse (2016) : the trajectory of test-masses is integrated assuming the star and the accretor are on circular orbits and that stellar rotation is synchronized with the orbital period. The 3D equation of motion in the co-rotating frame is :

$$\mathbf{v} \frac{d\mathbf{v}}{d\mathbf{r}} = \mathbf{a}_{\star} + \mathbf{a}_{\bullet} + \mathbf{a}_{\text{ni}} \quad (1)$$

where \mathbf{a}_{\bullet} stands for the acceleration due to the NS gravitational field and \mathbf{a}_{ni} for the non-inertial acceleration (centrifugal and Coriolis). The effective acceleration linked to the donor star of mass M_{\star} , once projected on the radial unity vector of the spherical frame of the star, is given by :

$$a_{\star} = -\frac{GM_{\star}}{r_{\star}^2} + a_{\text{rad}}(r_{\star}) + a_{\text{press}}(r_{\star}) \quad (2)$$

where a_{press} is the acceleration due to thermal and turbulent pressure, important near the stellar photosphere. For describing a_{press} and the total radiative acceleration a_{rad} , containing both the line and total continuum contribution, we rely on the computation by Sander, Fürst, Kretschmar, Oskinova, Todt, Hainich, Shenar and Hamann (2017) for Vela X-1. Using the stellar atmosphere code PoWR (Hamann and Koesterke 1998; Gräfener et al. 2002, e.g.), they calculate an atmosphere model for the donor star assuming a spherical, stationary wind situation. The radiative transfer is performed in the comoving frame, allowing to obtain the radiative acceleration without any further assumptions or parameterizations, i.e. :

$$a_{\text{rad}}(r_{\star}) = \frac{4\pi}{c} \frac{1}{\rho(r_{\star})} \int_0^{\infty} \kappa_{\nu} H_{\nu} d\nu \quad (3)$$

with c the speed of light and ρ the mass density, deduced from the stellar mass loss rate and the velocity using the conservation of mass. XXX ANDREAS : COULD YOU QUICKLY DEFINE KAPPA AND H? XXX Using the technique described in Sander, Hamann, Todt, Hainich and Shenar (2017), the model provides a hydrodynamically consistent stratification, meaning that the mass loss rate and the velocity field were iteratively updated such that eventually the outward and inward forces balance each other throughout the stellar atmosphere. The resulting velocity and density stratification shows notable deviations from the typically assumed β -law, especially within a couple of stellar radii, where the orbiting accretor lies and where the obtained wind velocity is lower than previously estimated (Gimenez-Garcia et al. 2016). Notice that in spite of the non-spherical situation due to the presence of the NS, we adopt a_{rad} as a_{press} as functions of the distance r_{\star} to the donor star here for the sake of simplicity.

The streamlines computation is performed using the code developed in El Mellah and Casse (2016), starting from the stellar surface whose ellipsoidal deformation, even for Roche lobe filling factors close to unity, is not included since it is expected to have a negligible impact on the formation of a wind-capture disc. An illustration of the result is given in Figure 1 where the streamlines have been represented in the orbital plane. We stop the integration when the test-masses reach a sphere around the accretor $\sim 30\%$ larger than its Roche lobe radius. This strategy alleviates the difficulty of an a priori estimate of the accretion radius (the critical impact parameter below which test-masses are captured in the BHL formalism, Edgar 2004). It delimits the space where the ballistic approximation no longer holds. Dissipative effects will be accounted for within this region in section 3. With this

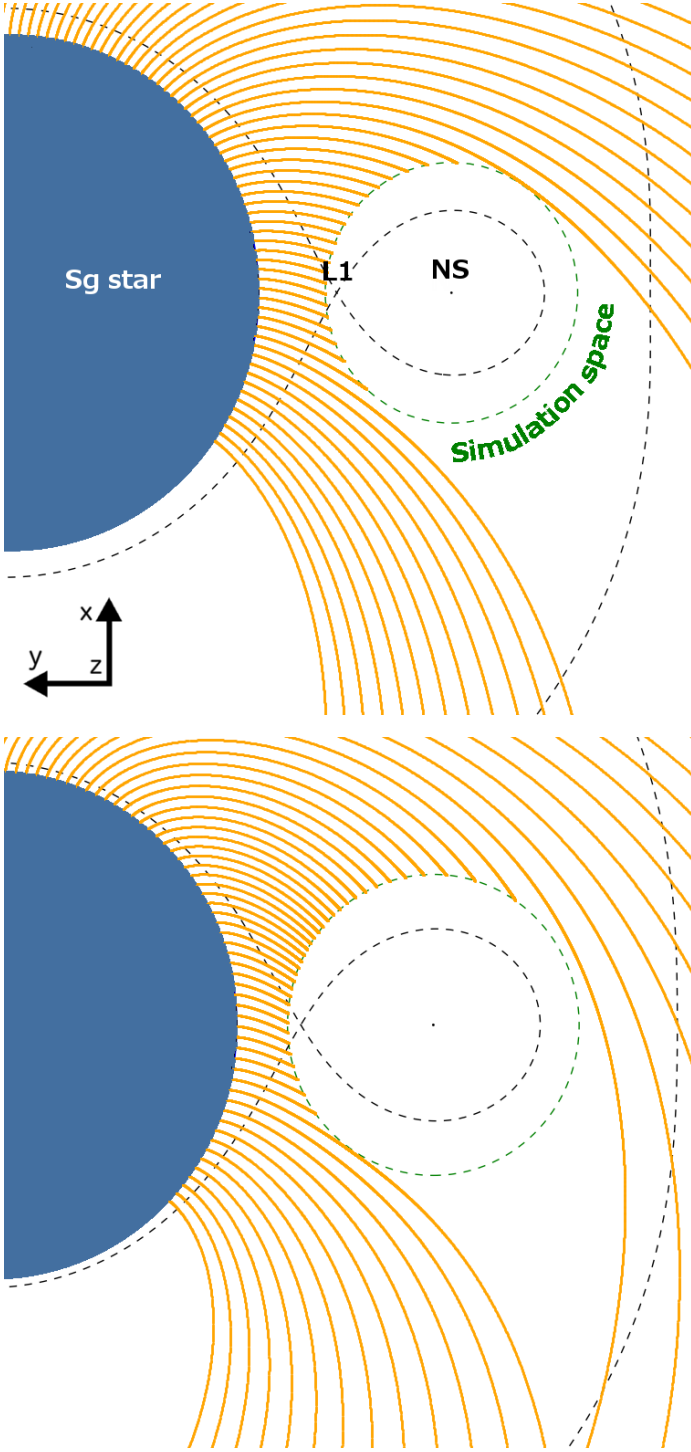


Fig. 1: In the orbital plane of the co-rotating frame, a few computed streamlines (orange) from the blue Sg to the HD simulation space (green dashed circle), centered on the accreting NS. The black dashed lines represent the critical Roche surface passing by the first Lagrangian point (L_1). Upper panel (resp. lower) is for the light fast (resp. heavy slow) configuration.

procedure, we focus on the fraction of the flow susceptible to be eventually accreted rather than on an accurate representation of the accretion tail in the wake of the accretor (for this component, see rather Manousakis et al. 2013).

Table 1: Parameters representative of Vela X-1 (with the star indexed with \star and the NS with \bullet) and integrated quantities at the outer edge of the simulation space for the 2 models considered.

	LF	HS
M_\star	20.2 M_\odot	
R_\star	28.4 R_\odot	
$P = 2\pi/\Omega$	8.964357 days	
a/R_\star	~ 1.8	
\dot{M}_\star	$1.3 \cdot 10^{-6} M_\odot \cdot \text{yr}^{-1}$	
M_\bullet	1.5 M_\odot	2.5 M_\odot
Boosted	Yes	No
$\dot{M}_{\text{out}}/\dot{M}_\star$	4%	17%
$l_{\text{out}}/a^2\Omega$	-1%	3%
$R_{\text{circ}}/R_{\text{mag}}$	4	30

Vink et al. (2001) showed that, provided the stellar effective temperature is larger than $\sim 25\text{kK}$, the wind terminal speed is expected to scale approximately as the effective escape velocity (i.e. once surface gravity has been corrected for radiative continuum pressure on free electrons via the Eddington parameter). Below this critical temperature, the terminal speed with respect to the effective escape speed of the star drops steeply. The donor star in Vela X-1, HD 77581, is a B0.5 Ib Sg star (Hiltner et al. 1972; Forman et al. 1973) whose effective temperature is of $\sim 25\text{kK}$. Gimenez-Garcia et al. (2016) suggested that it could explain the low terminal speed of $700\text{km}\cdot\text{s}^{-1} \pm 100\text{km}\cdot\text{s}^{-1}$ they measured for the wind of HD 77581. The computation carried on by Sander, Fürst, Kretschmar, Oskina, Todt, Hainich, Shenar and Hamann (2017) for HD 77581 also leads to terminal speeds ranging from 400 to $600\text{km}\cdot\text{s}^{-1}$ depending on the inclusion of X-ray illumination from the accretor. A decisive result of their analysis is that the latter modifies the ionization state of the metal ions in the wind but does not necessarily inhibit the acceleration process. On the contrary, far enough upstream the NS, the effective absorption of UV photons might be locally enhanced once the metal ions are in a higher ionization level. It is only close from the accretor, once all the elements have been deprived of their electrons, that the line-driven acceleration is halted, as previously emphasized in the literature (see e.g. Hatchett and McCray 1977; Ho and Arons 1987; Blondin et al. 1990; Karino 2014). XXX ANDREAS : DO YOU CONFIRM? WOULD YOU REFORMULATE? SHOULD IT BE AN ENTIRE SUBSECTION TO CLEARLY MAKE THIS POINT? XXX In an attempt to illustrate the dramatic impact of the efficiency of the line-driven acceleration on the subsequent properties of the accretion flow, and to encompass potential inaccuracies in the calculation of this acceleration in the context of Vela X-1, we consider the case of an artificially enhanced wind acceleration (by 50%) which leads to larger flow velocities by approximately 20%. In section 3, we will see that the orbital speed is a threshold which separates two types of accretion flows and given the value of the orbital speed in Vela X-1 ($\sim 284\text{km}\cdot\text{s}^{-1}$), this wind acceleration boosting will induce major changes. From now on, we consider the two cases in Table 1 :

- the heavy slow (HS) : the accretor is heavy, with a mass of $M_\bullet = 2.5M_\odot$, lying on the upper edge of the expected maximum mass for a NS, and the radiative acceleration is not boosted, leading to a relatively slow wind.
- the light fast (LF) : the accretor has a mass of $M_\bullet = 1.5M_\odot$ and the radiative acceleration is boosted by 50%.

Since the NS mass estimates in Vela X-1 range from $1.7M_{\odot}$ (Rawls et al. 2011) up to $2.3M_{\odot}$ (Quaintrell et al. 2003), partly due to the uncertainty on the inclination of the system, we expect the real configuration to lie in-between the two cases we consider.

2.2. Inhomogeneity and asymmetry of the wind

We now monitor the asymmetry and inhomogeneity of the flow when it reaches the spherical HD simulation space centered on the compact object and corresponding approximately to its Roche lobe. The aforementioned ballistic integration supplied information on the velocity vector at the surface of this sphere while the density relative to the one at the stellar photosphere is deduced from the divergence of each streamline. This information is then binned on angular tiles, with the polar axis of the spherical frame aligned with the orbital angular momentum axis (\hat{z} in Figure 1 and 2). In Figure 2, we represented Mollweide projections of the local mass and angular momentum inflow at the surface of this space for the HS and LF cases : it offers an overview of the properties of the flow entering the accretor Roche lobe, seen from the accretor.

Concerning the integrated values at the outer inflowing edge of the simulation space, we focus on the mass inflow rate, the net specific (i.e. per unit mass) angular momentum of the flow and its corresponding circularization radius. The latter is the radius at which a Keplerian orbit would have the same specific angular momentum. The values are given in Table 1 and compared respectively to the stellar mass loss rate \dot{M}_{\star} , to the orbital specific angular momentum $a^2\Omega$ and to the NS magnetosphere radius R_{mag} (see e.g. Frank et al. 1986) :

$$R_{\text{mag}} \sim 1.4 \cdot 10^9 \text{cm} \left(\frac{\rho}{10^{-12} \text{g} \cdot \text{cm}^{-3}} \right)^{-1/6} \left(\frac{v}{2,000 \text{km} \cdot \text{s}^{-1}} \right)^{-1/3} \dots \left(\frac{B_{\star}}{2.6 \cdot 10^{12} \text{G}} \right)^{1/3} \left(\frac{R_{\star}}{10 \text{km}} \right) \quad (4)$$

where the values used for the mass density ρ and the flow speed v are orders-of-magnitude at the outer edge of the magnetosphere. The low dependence of the magnetosphere radius on them guarantees that their exact value will not significantly alter this estimate. A typical NS radius has been used and the NS magnetic field is the one deduced by Fürst et al. (2014) in Vela X-1. In Table 1, we used $R_{\text{mag}} = 1.4 \cdot 10^9 \text{cm}$. We expect any disc-like structure to be truncated approximately at the inner radius (Ghosh and Lamb 1978) while quasi-spherical accretion onto the magnetosphere would proceed as described by Shakura et al. (2013). Notice that the mass inflow rates displayed in Table 1 set only upper limits on the final rate at which matter will be accreted since only a subset of the streamlines entering the Roche lobe of the accretor will eventually be accreted. However, it is already striking to notice how much more important is the fraction of the stellar wind entering the simulation space in the HS configuration compared to the LF one. The difference is essentially due to a significantly more important contribution of the high latitude region in the former case. Concerning the angular momentum, it might still vary within the simulation space since the forces are not isotropic around the accretor. The results displayed in Table 1 serve to show that, within the current uncertainties on the mass of the accretor and on the efficiency of the wind launching process in Vela X-1, the 2 cases lead to dramatically different accretion flow configurations, in spite of their apparently similar parameters. In the HS case, where the flow is slightly slower than the orbital speed, the mass inflow rate within the Roche lobe of the accretor is 4 times larger, while the circularization radius is

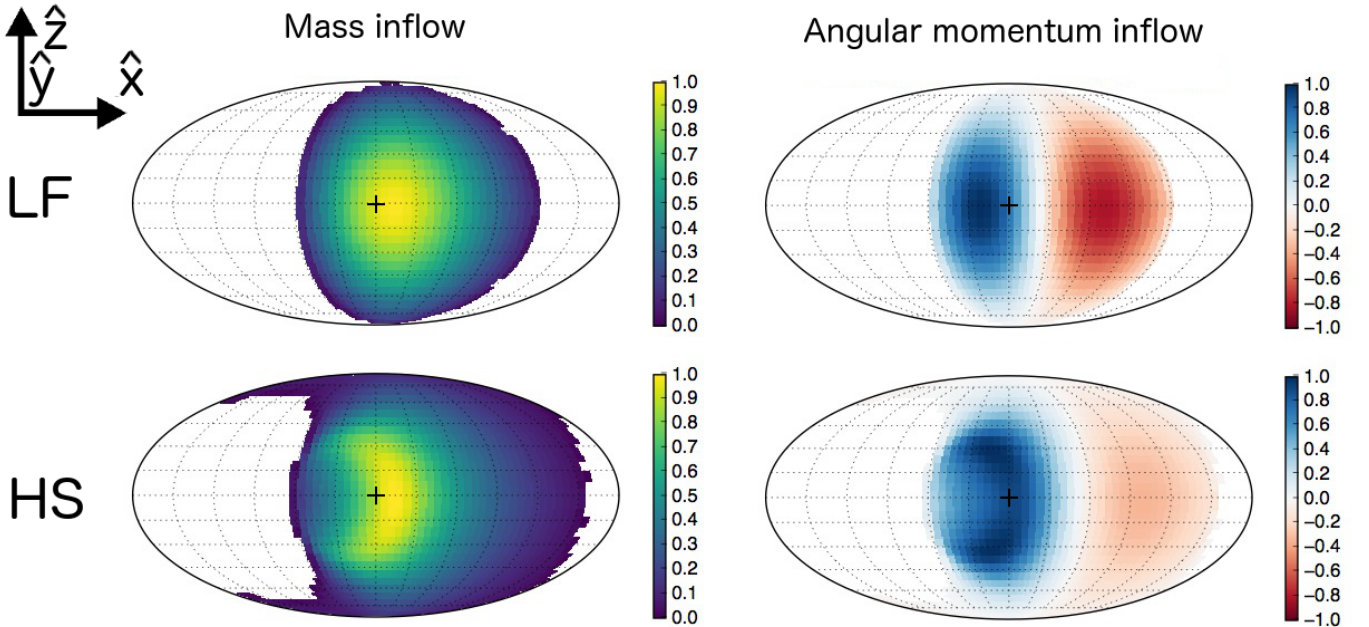


Fig. 2: Mollweide projections of local mass and angular momentum inflows within the simulation space centered on the accretor (dashed green sphere on Figure 1). The upper row corresponds to the light fast (LF) case while the bottom row is for the heavy slow (HS) case. Each map is scaled to its maximum (absolute) value and centered on the axis from the accretor to the donor star (central dark cross). Positive (resp. negative) values of angular momentum stands for locally prograde (resp. retrograde) flow with respect to the orbital motion.

almost an order of magnitude larger than in the LF case, where the flow is slightly faster than the orbital speed.

On the left panels in Figure 2, we see that the bulk of the mass inflow is approximately distributed in the same way in both cases, with a larger off-plane contribution when the wind is slower : it is a first hint that the inertia of the wind is no longer large enough to overcome the orbital flattening induced by rotation, a feature which will have major consequences within the shocked region. In both cases, the incoming flow is centered around a mean radial direction which departs from the axis joining the compact object to the star (central cross in Figure 2). The main difference though lies in the distribution of angular momentum inflow (right panels) : the LF case leads to an equivalent amount of positive and negative angular momentum, revealing of the essentially planar (albeit deviated) structure of the flow, whereas the HS case displays a large unbalance. The evaluation of the net angular momentum inflowing was in no case obvious a priori : the flow arriving from the first Lagrangian point L_1 (with positive angular momentum) is denser than the flow arriving from the right of L_1 as seen from the accretor (with negative angular momentum), but it is also slower. The present analysis shows that the former effect eventually dominates. The non-zero net angular momentum in the HS case can not be attributed to an asymmetry of the mass inflow. Rather, it is due to the shift between the mean direction of arrival of matter (yellow spot in mass inflow maps) and the direction of radial inflow (white stripe in-between blue and red in angular momentum inflow maps). It is much more significant for HS than for LF. Consequently, the net amount of specific angular momentum is larger for HS, which also leads to larger circularization radii and to the likelier presence of a wind-capture disc, a prediction we now put to the test.

3. Wind-capture discs

3.1. Physics and numerical setup

3.1.1. Equations

Within the Roche lobe of the accretor, we solve the HD equations in their conservative form, converting accordingly the gravitational, radiative and non-inertial accelerations in the ballistic equation of motion (1) into forces per unit volume. In a first time, we do solve the energy equation everywhere, assuming that the heating from the donor star and from the X-rays produced in the vicinity of the accretor balances the cooling of this optically thin supersonic wind. In section 3.1.2, we will discuss the validity of this adiabatic approximation downstream the shock which will form, and a way to relax it. Finally, we complement these equation with the equation-of-state of an ideal monoatomic gas of Hydrogen (i.e. with an adiabatic index $\gamma = 5/3$), which gives the internal energy per unit volume u as a function of the thermal pressure P only.

The computation is performed with the new version of the finite volume code MPI-AMRVAC (Xia et al. 2018), using a 3rd order HLL solver (Toro et al. 1994) with a Koren slope limiter (Vreugdenhil and Koren 1993). The spherical mesh we set up is an extension of what has been developed for an axisymmetric 2D flow in El Mellah and Casse (2015) : it is centered on the accretor and radially stretched to guarantee a constant relative resolution from the outer to the inner edge of the simulation space, spanning several orders of magnitude at an affordable computational cost and with a uniform cell aspect ratio. The outer radius of the simulation space is approximately half of the orbital separation,

which is $\sim 0.2\text{AU}$ in Vela X-1, while the inner edge has a radius of 5 times the NS magnetosphere radius given by equation (4), hence a factor of approximately 200 between the inner and outer edge. Due to the symmetry of the problem above and below the orbital plane, we consider only the upper hemisphere and work with a resolution of $128 \times 32 \times 128$ corresponding to cells of aspect ratio close to unity near the equatorial plane of the mesh. Since our aim is to identify the conditions suitable for the formation of a wind-capture disc, the conservation of angular momentum is of uttermost importance. We implemented an angular momentum preserving scheme which guarantees the conservation of the component of the angular momentum projected onto the polar axis, in particular in the innermost regions of the flow, to machine precision (XXX RONY : WOULD YOU HAVE A REFERENCE IN MIND? XXX). However, we confirm that our results remained essentially unchanged by setting the polar axis in the orbital plane (but still orthogonal to the line joining the star to the compact object i.e. along the \hat{x} axis), which empirically verifies that MPI-AMRVAC properly handles the polar singularity.

3.1.2. Radiative cooling

Let us estimate the importance of cooling in this physical environment. Upstream the shock, we rely on the temperature stratification derived from the solution of the statistical equilibrium equations and the radiative transfer. Based on the assumption of radiative equilibrium, the (electron) temperature structure in an expanding atmosphere is obtained by applying a generalized Unsöld-Lucy method described in Hamann and Koesterke (1998). Including the X-ray irradiation on the donor star did not significantly alter the temperature profile upstream the accretor obtained in Sander, Fürst, Kretschmar, Oskanova, Todt, Hainich, Shenar and Hamann (2017), leading to wind temperatures of 15 to 20kK. XXX ANDREAS : DO YOU CONFIRM THE CONTENT AND THE FORM? XXX. Downstream the shock, we assume that the gas is still optically thin and write the time scale τ_c to evacuate the internal energy per unit volume of an ideal gas at temperature T and with a Hydrogen number density n , $u = nk_B T$, at a rate given by the cooling rate computed by Schure et al. (2009), $\Lambda(T)$:

$$\tau_c = \frac{nk_B T}{n^2 \Lambda(T)} \quad (5)$$

where Λ includes the proportion of electrons relative to protons and k_B is the Boltzmann constant. If we write τ_d the dynamical time scale for free fall at a fiducial accretion radius R_{acc} of $1/30^{\text{th}}$ of the orbital separation in Vela X-1, we obtain the following ratio :

$$\frac{\tau_c}{\tau_d} \sim 0.01 \left(\frac{T}{10^6 \text{K}} \right) \left(\frac{\Lambda}{10^{-22} \text{erg} \cdot \text{s}^{-1} \cdot \text{cm}^3} \right)^{-1} \dots \quad (6)$$

$$\dots \left(\frac{\rho}{10^{-13} \text{g} \cdot \text{cm}^{-3}} \right)^{-1} \left(\frac{M_\bullet}{2M_\odot} \right)^{1/2} \left(\frac{R_{\text{acc}}}{0.2\text{AU}/30} \right)^{-3/2} \quad (7)$$

where we used the values of temperature and density measured downstream the shock in the adiabatic simulations presented in section 3.2.1. It is clear that, except if the wind is a few times faster than expected in Vela X-1 and/or the star displays a mass loss rate an order of magnitude lower than what models and observations indicate ($\sim 1.3 \cdot 10^{-6} M_\odot \cdot \text{yr}^{-1}$, Gimenez-Garcia et al. 2016), the flow will be dense enough to significantly cool in the shocked region.

In an optically thin environment, we could include radiative cooling using the module developed for MPI-AMRVAC by van

Table 2: Parameters of cooling prescriptions in the four models.

	adiabatic	isoS	Hot	Cool
Cooling	no	yes	yes	yes
T_0	–	10^6K	10^6K	10^5K
C	–	S_0	T_0	T_0
α	–	γ	1	1

Marle and Keppens (2011). However, we would also need to model heating by X-rays from the compact object and by the stellar radiation field, and to use power-law approximations to compute the local opacity as a function of the density and the temperature (Lin and Papaloizou 1985). Besides, the optically thin approximation might not hold within the shocked region, especially when runaway cooling occurs and a high density disc-like region forms. In optically thick regions, the strong coupling between matter and radiation requires more sophisticated treatments such as flux-limited diffusion (Turner and Stone 2001). XXX RONY : SHOULD WE CITE JANNIS' PAPER HERE? XXX Given the additional layers of complexity a proper treatment of radiation would add, we chose to represent the cooling in a simpler way, using a polytropic model. It is equivalent to assume that the ratio of energy radiated away by the work done by the pressure force is constant : a certain compression leads to a certain energy loss, ranging from 0 (in the adiabatic limit) to 100% (in the isothermal limit) of the work done by the pressure force (Christians 2012). Above a certain threshold temperature T_0 , reached only within the shocked region, we overwrite the solution for the internal energy computed by the energy equation with the corresponding value of pressure deduced from the polytropic relation :

$$P = C\rho^\alpha \quad (8)$$

Provided there is no creation of entropy (in particular no shock), C is constant and uniform. In this framework, the polytropic index α ranges from 1 in the isothermal limit to γ in the adiabatic limit (Horedt 2000). After exploring a range of realistic values for C and α , we retained 3 different cooling models :

- Isoentropic (or "isoS") : cooling occurs only in a thin unresolved radiative layer immediately downstream the shock and is then negligible (for instance, because of intense X-ray heating) which means $\alpha = \gamma$ and a constant C set to a fraction of the entropy the flow would acquire downstream the shock in the fully adiabatic case, S_0 . T_0 is set to 10^6K .
- Isothermal hot (or "hot") : above $T_0 = C = 10^6\text{K}$, the net cooling is efficient enough to compensate any adiabatic compression as the flow accretes, which leads to an isothermal flow ($\alpha = 1$).
- Isothermal cool (or "cool") : same as previous but with a temperature $T_0 = 10^5\text{K}$.

In the two isothermal cases, the cooling prescription means that the flow evolution is fully adiabatic until it reaches the temperature $T_0 = C$ when it becomes isothermal. We believe that including the optically thin cooling without heating would lead to results qualitatively similar to the isothermal prescription we introduce here (as noticed by Saladino et al. 2018) . The four models (fully adiabatic, isentropic, isothermal hot and cool) are summarized in Table 2.

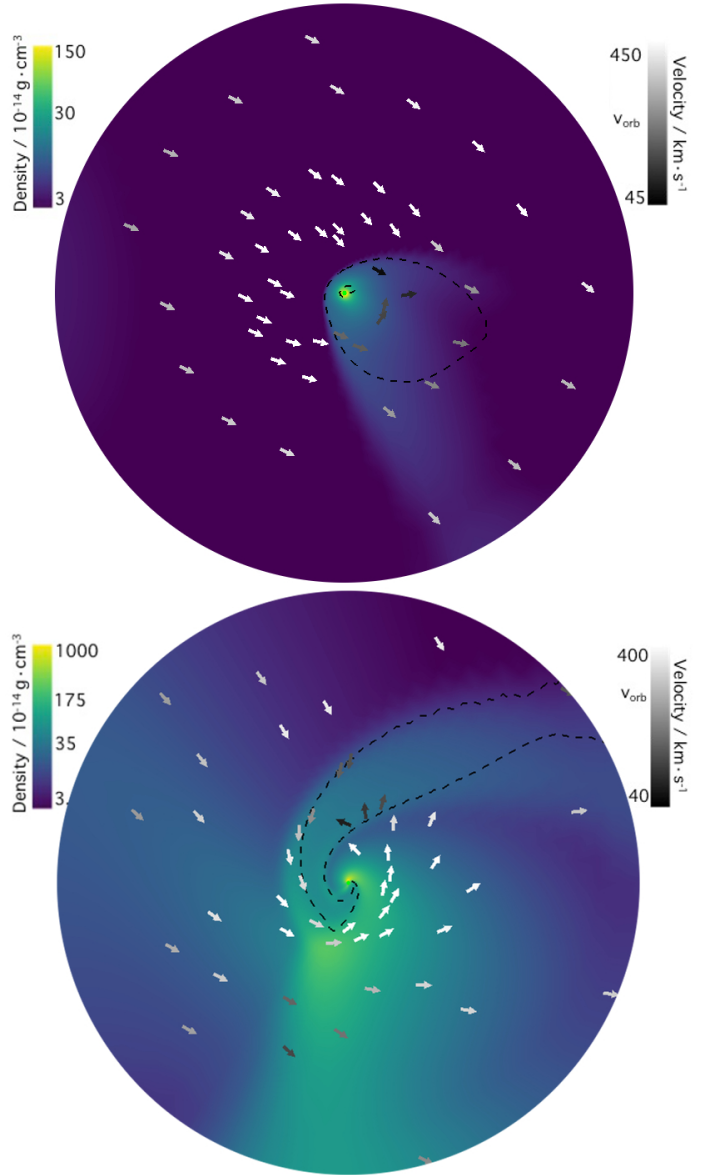


Fig. 3: Logarithmic colormaps of the density field in the orbital plane. The arrows stand for the velocity field, with a black to white colormap for their increasing magnitude. The orbital speed of Vela X-1, $v_{\text{orb}} \sim 284\text{km}\cdot\text{s}^{-1}$, has been represented (linear scale). The black dashed line is the Mach-1 contour. The radial extension of the simulation domains relative to the orbital separation corresponds to the green dashed delimited regions in Figure 1, which is approximately the Roche lobe of the accretor. (bottom) LF configuration. (top) HS configuration.

3.2. Flow morphology

3.2.1. Adiabatic evolution

In Figure 3, we represented slices in the orbital plane of the numerically relaxed state reached by the simulations where the adiabatic HD equations are solved. A 3D representation is displayed in Figure 4 to appreciate the level of beaming of the flow in the orbital plane.

In the case of a light accretor capturing material from a fast wind (LF configuration, upper panel in Figure 3), the main features depart little from what has been observed for axisymmetric uniform flows. In agreement with Blondin and Raymer (2012),

we do not observe any transverse oscillation of the tail (the so-called "flip-flop instability" which arises mostly in 2D polar numerical setups, Foglizzo et al. 2005). The orbital effects deflected the wind whose mean direction of arrival is ~ 20 degrees misaligned with respect to the axis joining the star to the compact object. However, as discussed in section 2.2, the flow remains essentially planar around this direction. When the flow is sufficiently beamed towards the accretor, it forms a bow shock (semi-transparent blue surface in Figure 4) at a distance ahead the accretor compatible with a fraction of the accretion radius (Edgar 2004). The Mach-1 surface and the cone of density jump are slightly misaligned with each other, with the side facing the star denser. The Mach number immediately upstream the shock reaches 30 and we retrieve the classic jump conditions for an adiabatic shock. Between the outer boundary upstream and the inner boundary, the density (resp. the temperature) increases by a factor of ~ 100 (resp. 5,000). In the innermost regions of the flow, we retrieve the sonic surface though no longer anchored into the inner boundary, contrary to what was predicted for a planar uniform flow with $\gamma = 5/3$ by Foglizzo and Ruffert (1996).

In the case of a heavy accretor capturing material from a slow wind (HS configuration, lower panel in Figure 3), the morphology of the flow is dramatically different. Not only is the mean direction of arrival of the flow more misaligned with the line joining the star to the compact object (~ 45 degrees) but also the shearing is much more important, leading to a significant amount of net angular momentum. A bow shock also forms but while it extends over several accretion radii on the side where the flow is less dense and faster, the beamed wind arriving directly from L_1 remains mildly supersonic as it passes the accretor. It is strongly deflected and accelerated by the gravitational slingshot but only to finally impacts the shocked region from the back. The adiabatic compression it first experiences leads to a dense and fairly cool region compared to the innermost parts of the flow. We also notice that when the wind is slower, material from higher latitudes on the star contributes to the accretion process, as shown by the vertical extent of the mass inflow map in Figure 2 : its beaming in the orbital plane builds up the red dark bulge observed on the right in Figure 4. It is a specific feature of wind RLOF configurations since in pure RLOF, only matter from the vicinity of L_1 flows in the Roche lobe of the accretor while in pure wind configurations, the centrifugal force is too weak to focus the fast wind in the orbital plane and the wind at high stellar latitude do not participate neither to the accretion process. Downstream this bulge, as seen in Figure 4, the shocked region of the HS setup presents a characteristic spiral shape which delimits a narrow accretion channel along which matter flows in (or out beyond the stagnation point). The orientation of this stream differs in its orientation with the one observed in RLOF systems due to the much lower effective gravity of the donor star (after including the line and pressure accelerations), which alters the classic Roche potential we rely on in LMXB.

Although the Mach number of the flow entering the simulation space remains below 10 due to the limited efficiency of the wind acceleration, it reaches Mach numbers of 20 just upstream the shock, leading to a temperature jump of approximately 400. As the flow is accreted, the corresponding temperatures of the order of 10MK keeps increasing up to 100MK at the inner boundary. In the absence of radiative cooling, these temperatures are to be expected but as explained in section 3.1.2, the density of the flow is too high to neglect its capacity to radiate internal energy away.

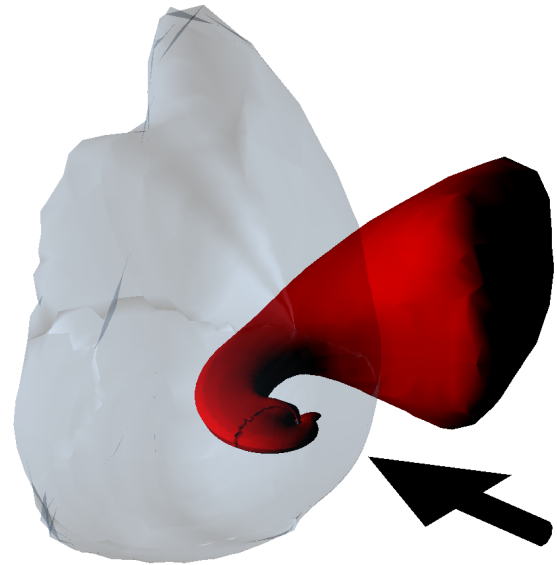


Fig. 4: 3D contours of the mass density for the LF (semi-transparent blue) and HS (red) configurations. The black arrow indicates the approximate direction of the arriving wind, while the vertical direction is aligned with the orbital angular momentum. Notice the axisymmetry of the LF flow structure around the mean direction of wind arrival, whereas the HS flow is compressed in the orbital plane and forms a characteristic channel reminiscent of the stream of matter in RLOF systems. Same scale as Figure 3.

3.2.2. Polytropic cooling

The case for cooling has been made in section 3.1.2 on the base of preliminary estimates. Let us now study its influence on the morphology of the flow in the LF and HS cases.

Whatever the cooling prescription invoked, the LF setup never leads to the formation of a disc-like structure around the accretor. Instead, triggering the cooling for the LF flow leads to a serious recession of the front shock, down to the inner boundary of the simulation space, due to a drop of the pressure built-up downstream the shock. With the isentropic prescription, we ran a simulation with an inner boundary 5 times smaller to make sure that the size of the inner boundary was not impacting the morphology of the flow, and the result remained unchanged. Since the magnetic field is believed to play a role so close from the accretor and our simulations are only HD, we are not able to make any statement on the following accretion of the flow in the LF case, except that it is bound to not proceed via a disc. From now on, "LF" refers to the LF configuration coupled with the isentropic cooling prescription.

On the contrary, in the HS configuration, the front shock holds and a permanent disc-like structure forms within the shocked region, whatever the cooling prescription used (see Figure 5). In the isentropic case, the hull of the shock remains essentially unchanged, including the density bulge, since the cooling is only triggered in the innermost region, where the temperature of the flow goes beyond $T_0 \sim 1\text{MK}$. There, we do observe the formation of a flattened persistent structure, partly supported by the centrifugal force (see Figure 6). As indicated by the relatively large thickness aspect ratio of the disc (~ 0.5), the pressure still plays an important role in sustaining the structure. Similarly, this disc-like structure appears in the two isothermal cases, with a thinner disc for a lower temperature. From now on, "cool",

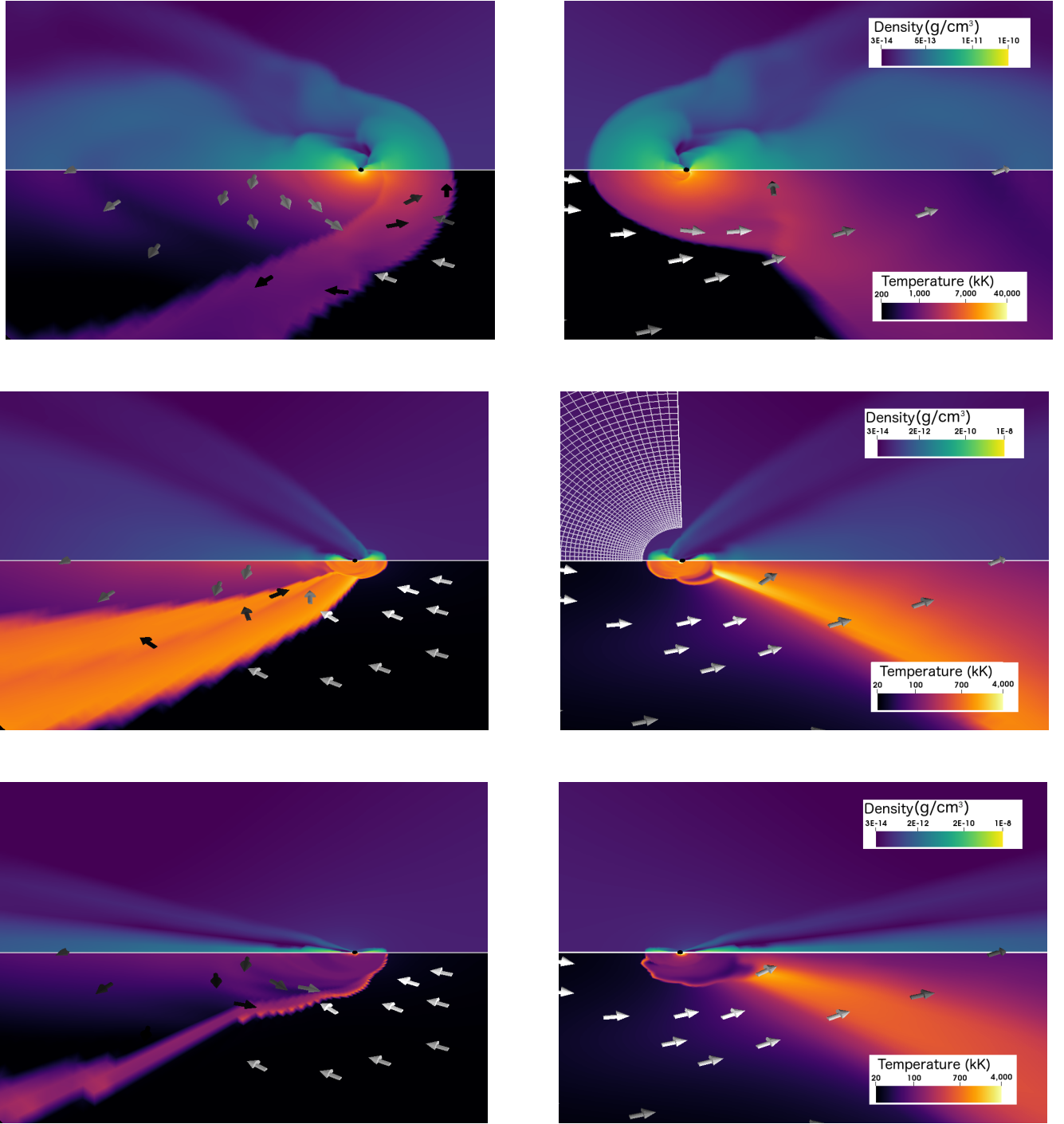


Fig. 5: Side-views of the flow structure when cooling is triggered using an isentropic (upper panels) or an isothermal prescription, with a high temperature (middle) or low temperature (lower panels). In the left (resp. right) column, the wind comes from the right (resp. left). The lower half of each panel displays a logarithmic thermal colormap in the orbital plane while the upper half represents the transverse (or "vertical") logarithmic density distribution. We also plotted the velocity field in the orbital plane, with white to black color scale to indicate a slowing down by a factor of at least 4. The radially stretched mesh has been represented to indicate the resolution.

"hot" and "isoS" refer to the HS configuration coupled with the corresponding cooling prescription.

Another way to appreciate whether the flow is centrifugally supported and up to which radius is to plot the longitudinal velocity profile in the orbital plane. In Figure 7, it appears clearly that the LF case displays a flow speed (solid blue line) highly below the Keplerian expectation (dashed blue), while the three HS

cases show a much better matching between the measured (red, green and orange solid lines) and the Keplerian (black dashed) velocity profiles. Within the disc, the velocity profile is a power-law (the profiles are straight lines) but once we reach the outer extent of the disc, a sudden change in slope happens. A warmer disc corresponds to a larger extent of the disc. While the two isothermal cases decreases in $1/\sqrt{r}$ (in agreement with a con-

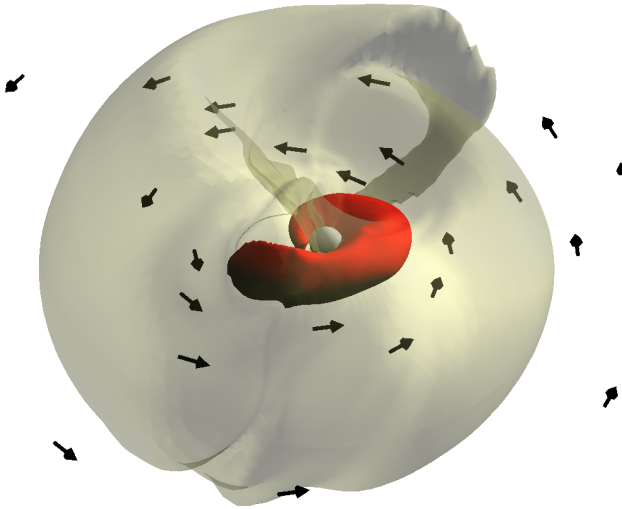


Fig. 6: 3D contours of the mass density for the isentropic HS configuration (upper panels in Figure 5), with the yellow semi-transparent surface 5 times less dense than the inner red surface. The arrows stand for the velocity field in the orbital plane. The flow comes from the upper left. Spiral arms are visible for each surface. The central white sphere stands for the inner boundary of the simulation space, ~ 200 times smaller than the outer boundary displayed in Figure 1.

stant temperature and a power-law density profile), we notice that they are both offset from the Keplerian profile. They display rotational speed approximately 15% above the Keplerian speed within the disc, which is partly due to the longitudinal arithmetic mean at a given radius which favors the larger values. It might also be due to numerical effects at the inner border or representative of a non-fully steady numerical state (see section 4.1). In the isentropic case, we observe a velocity profile decreasing faster than $1/\sqrt{r}$ which indicates an increasing importance of the thermal pressure in the equilibrium of this thicker disc.

Without cooling, we have seen that no disc formation is possible, whatever the net angular momentum carried by the accreted flow. It agrees with previous 3D numerical simulations of asymmetric BHL accretion, either in the context of common envelope phase (MacLeod and Ramirez-Ruiz 2014) or mass transfer in binaries where the donor star is on the asymptotic giant branch (Saladino et al. 2018). More generally, without energy loss, a flow with a given angular momentum can not circularize. By analogy with a test-mass, it would keep orbiting on the highly eccentric orbit the initial conditions imprinted. The shock mediates this analogy by adding entropy to the flow, but internal energy needs to be radiated away to lead to the formation of a centrifugally supported structure.

4. Discussion and observational consequences

4.1. Accretion rates

4.1.1. Mass accretion rate

After at most a few crossing times, the total mass and angular momentum within the simulation space reach a plateau and the mass and angular momentum accretion rates do not vary by more than a few percents. The levels we observe depend significantly

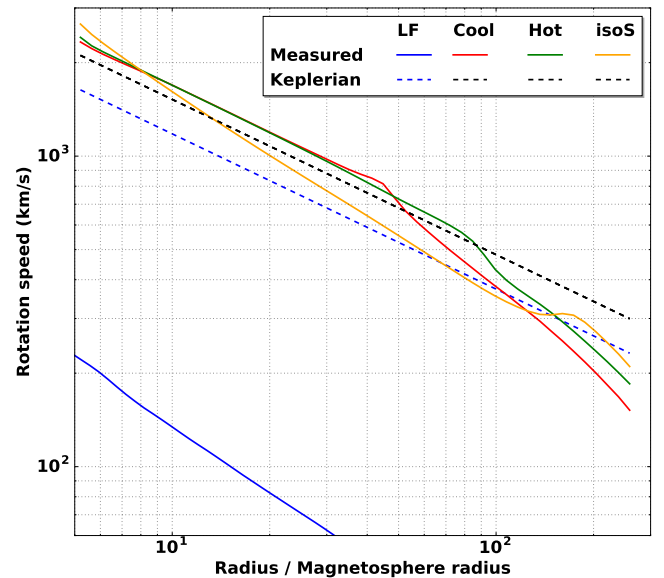


Fig. 7: Longitudinal velocity profiles in the orbital plane as a function of the distance to the accretor measured in units of the magnetosphere radius given in equation (4). The velocities have been measured once the numerically relaxed state has been reached and have been averaged over the longitudinal angles. The measured velocity (solid lines) are compared to the Keplerian profile expected for a thin disc (dashed).

on the efficiency of the wind line-driven acceleration and of the mass of the accretor (LF and HS configurations). In Figure 8, we represented the mass accretion rate at the inner boundary of the simulation space as a function of time. Comparing the HS and LF cases enables us to underline the dramatic increase in the mass accretion rate when the acceleration provided to the wind leads to a specific kinetic energy of the order of the Roche potential of the binary system at the first Lagrangian point (i.e. a similar wind speed compared to the orbital speed). While the mass entering the Roche lobe of the accretor was approximately 4 times larger in the HS case (see section 2.2), the mass flows within a sphere of a few times the NS magnetosphere radius at a rate an order of magnitude larger in the HS case compared to the LF one. The mass accretion rates displayed in Figure 8 are steady and, within the shocked region, fairly independent of the radius at which they are measured, in agreement with the conservation of mass.

Currently, accretion of matter within the inner border is enabled only by the evacuation of angular momentum through spiral shocks (visible in Figure 6). However, in the absence of a proper treatment of the effective viscosity, statements on the absolute values of the mass accretion rate witnessed in these simulations should be taken with caution. That being said, the values we observe, of the order of a few $\dot{M} \sim 10^{-8} M_{\odot} \cdot \text{year}^{-1}$ would correspond to X-ray accretion luminosities of the order of $L_{\text{acc}} \sim \eta \cdot 3 \cdot 10^{39} \text{ erg} \cdot \text{s}^{-1}$, where η encapsulates the information on the efficiency of the conversion process from kinetic energy to X-ray emission. Provided this coefficient reaches its maximum value given by the compactness parameter of the accretor (10 to 30% for a NS), the X-ray luminosity would be an order of magnitude higher than the Eddington luminosity L_{Edd} of a NS. In this case, the cooling prescriptions we relied on would break up and a more rigorous treatment of the radiative feedback would be required to make reliable conclusions. Interestingly enough,

it means that wind-RLOF, because it combines both the mass transfer efficiency of RLOF (usually associated to LMXB) and the large amount of available matter provided by the mass loss mechanism of a massive star (associated to HMXB), could lead to super-Eddington accretion. In particular, we notice that some Ultra Luminous X-ray sources (ULX) have been shown to be super-Eddington accreting NS (Bachetti et al. 2014; Fürst et al. 2016; Israel et al. 2017) but the only stellar companion whose spectral type has been identified among this NS-ULX is a B9Ia (Motch et al. 2011), presumably too cold to display the required mass loss rate XXX JON, ANDREAS, WHAT IS YOUR OPINION HERE? DO YOU CONFIRM? THERE IS ALSO A WR STAR IDENTIFIED IN M101 ULX, MORE SUITABLE TO PROVIDE LARGE AMOUNTS OF MASS, BUT NO NS SIGN TO MY KNOWLEDGE XXX.

Regarding the current systems of interest in this paper, classic SgXB and Vela X-1 in particular, it would be inconsistent with the observed X-ray luminosity ranging from $10^{35}\text{erg}\cdot\text{s}^{-1}$ to a few $10^{37}\text{erg}\cdot\text{s}^{-1}$ in Vela X-1 (Fürst et al. 2010). In the case of an accreting black hole, very low values of η can be reached for radiatively inefficient accretion flow, either because the flow has no time to cool or because it is optically thick enough to drag the radiation in its fall towards the event horizon (Narayan et al. 1998). But for a NS, the kinetic energy must be released before or at the impact with the NS surface (Medvedev and Narayan 2000). Very faint accreting NS have been identified in LMXB (Armas Padilla et al. 2013). In spite of a RLOF mass transfer susceptible to provide a large fraction of the Eddington mass accretion rate, these systems maintain low X-ray luminosities of $5\cdot 10^{34}$ to $5\cdot 10^{36}\text{erg}\cdot\text{s}^{-1}$ (i.e. 10^{-4} to $10^{-2}L_{\text{Edd}}$) for years, much below the levels generally observed in LMXB. Degenaar et al. (2017) reported about observational signatures of an outflow in one of these sources, IGR J17062–6143, and suggested two mechanisms to account for the low luminosity of the accreting NS. The first possibility could be a truncated disc with a radiatively-inefficient accretion flow in the inner parts (see e.g. the adiabatic inflow-outflow solution derived by Blandford and Begelman 1999), possibly associated with an outflow. An alternative scenario is a propeller-driven outflow. In the regions where we monitored the flow, the magnetic field carried by the flow has little influence on the motion of the gas. However, when the flow gets close enough from the accretor, it gets highly ionized by the X-ray emission and encounters the intense dipolar magnetic field of the NS. From this point, the magnetic field takes over and controls the dynamics : in SgXB, any putative disc-like structure would eventually be truncated way before the NS surface (Ghosh and Lamb 1978). In the propeller regime, part of the matter falling onto the magnetosphere might eventually be repelled, leading to a much lower effective mass accretion rate than the amount inflowing at a few magnetosphere radii (Illarionov and Sunyaev 1975; Bozzo et al. 2008).

—
→ XXX Any outflow observed in Vela X-1? XXX
—

4.1.2. Angular momentum accretion rate

When a disc forms, the angular momentum accretion rate at a few R_{mag} can in no case be indicative of the torque applied to the accretor since it is precisely thanks to the evacuation of a significant amount of angular momentum that accretion takes place. However, it provides an upper limit which can be computed to monitor the consistency of these simulations. In addition, the specificities of the exchange of angular momentum be-

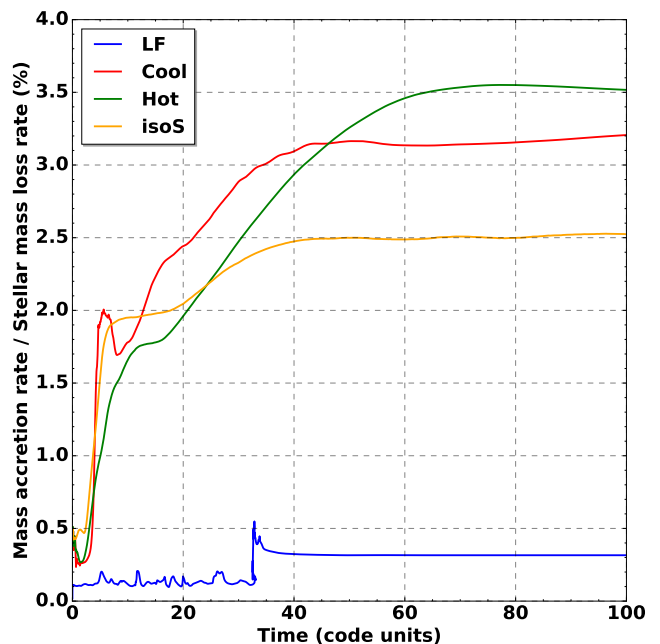


Fig. 8: Mass accretion rates at the inner border of the simulation space (at $\sim 5R_{\text{mag}}$) as a function of time. In the case of the HS configuration, the mass accretion rate is significantly larger than in the LF case, whatever the cooling prescription.

tween the flow and the NS depends on the extent of the corotation radius with respect to the magnetosphere radius (Ghosh and Lamb 1979). A naive computation of the characteristic spin-up time τ_L of a NS of mass $M_\bullet = 2M_\odot$, of radius $R_\bullet = 10\text{km}$ and of spin period $P_\bullet = 2\pi/\omega = 283\text{s}$, representative of the one hosted in Vela X-1, would give, with the angular momentum accretion rate \dot{L} we measure at the inner edge of the HS simulations :

$$\tau_L = \frac{L_\bullet}{\dot{L}} = \frac{M_\bullet R_\bullet^2 \omega_\bullet^2}{\dot{L}} \sim 10\text{kyrs} \quad (9)$$

which is one to three orders of magnitude smaller than the net spin-up/down time observed reported in the literature (see e.g. Ziolkowski 1985). It shows that the angular momentum flowing through the inner boundary of our simulation space is in excess and that only a fraction will play a role in the spinning-up/down of the accreting NS.

4.2. Disc extension and viscous lag : the case of Cygnus X-1

Even in systems which are known to harbor an accretion disc, we have often little insights on the disc outer radius. Indeed, most of the light comes from the innermost region, which are also, for a disc extending all the way down to the compact accretor, the ones emitting in X-rays, in a waveband well separated from the stellar black body emission. In RLOF systems, the monitoring of the hot spot can help to locate this outer ring, provided the disc is not tilted, and theoretical limits exist on the maximum extension of the disc ($\sim 70\%$ of the Roche lobe radius of the accretor, Paczynski 1977).

Recently, Taam et al. (2018) invoked a hot, low angular momentum accretion flow to explain the absence of visible hysteresis in the hardness-intensity cycle of Cygnus X-1, where the contrast is low between the brightest and dimmest X-ray emission compared to BH in LMXB (Grinberg et al. 2014). Indeed, in Cygnus X-1, mass transfer most likely proceeds through wind

accretion. The present study, although focused on the case of a NS accretor, indicates that, if the wind speed is not negligible compared to the orbital speed, the disc should be smaller than what a RLOF process would produce in a classic BH-LMXB. In Cygnus X-1, the donor star is of similar mass as in Vela X-1 but with a radius smaller by almost a factor of 2 (Orosz et al. 2011), which would lead, for a similar Eddington parameter, to a larger wind terminal speed if it scales as the effective escape speed at the stellar photosphere (as discussed in section 2.1). But this increase must be compared to the orbital speed in Cygnus X-1 ($\sim 400 \text{ km s}^{-1}$) which is also larger than in Vela X-1, and to the much more important mass of the accretor relative to the donor star. All in all, the extent of the wind-capture disc formed in Cygnus X-1 might be larger than observed in the HS configuration, more suitable for Vela X-1, but much smaller than a RLOF formed disc. Smith et al. (2001) already pinpointed that the delay between the hard to soft and soft to hard transitions might be representative of the different propagation times in a two components accretion flow : while the corona reacts to a perturbation of a free-fall timescale, the disc, limited by the viscous timescale, would always lag behind. Because the viscous timescale depends on the outer extent of the disc, a lower delay in the hardness-intensity cycle of Cygnus X-1 compared to BH-LMXB would indicate a smaller disc extent, consistent with the present study of the properties of wind-capture discs.

5. Conclusion

In this paper, we tried to evaluate the possibility to obtain a wind-capture discs in SgXB and in particular in the classic NS-hosting SgXB Vela X-1. We connected the orbital scale, at which the wind unfolds, to the one of the accretion radius, at which the flow is significantly beamed by the gravitational field of the compact object and where HD shocks form, all the way down to the outer edge of the NS magnetosphere. It enables us to consistently embrace the development of the wind as it is launched, compute its deviation at the orbital scale and evaluate the fraction eventually reaching the NS magnetosphere. We showed that the wind dramatically departs from a radial outflow when the stellar line-driven acceleration leads to velocities at the first Lagrangian point connecting the two Roche lobes similar to or lower than the orbital speed. We also capture the adiabatic bow shock which forms ahead of the accretor and characterize its highly asymmetric shape for a slow wind. Provided cooling is triggered in the shocked region, the accreted flow formed out of a slow wind circularizes at a few 10 times the NS magnetosphere radius. The obtained disc-like structure is essentially maintained by the centrifugal force and displays a quasi-Keplerian rotation profile.

Currently, we face a lack of conclusive evidence in favor of the presence of a permanent disc in SgXB hosting NS (Bozzo et al. 2008; Shakura et al. 2012; Romano et al. 2015; Hu et al. 2017). Yet, because of the truncation of the disc by the NS magnetosphere (Ghosh and Lamb 1978), we do not expect from it an emission as intense and as high energy as for a disc extending deeply into the gravitational potential of the compact accretor. In UV waveband, the emission from a putative disc would be dominated by the flux from the O/B Sg star and in the X-rays, accretion columns at the NS poles would be much brighter than the truncated disc. Alternatively, if the wind actually reaches speeds larger than the orbital speed upstream the accretor, a wind-capture disc would be ruled out by the present study.

To summarize, in Vela X-1, we face two possible wind accretion scenarios :

- the line-driven wind acceleration is not efficient enough to provide the flow with a velocity larger than the orbital speed when it enters the Roche lobe of the accretor. In this case, the orbital effects control the dynamics of the wind which is seriously beamed, with a fraction of the stellar mass loss rate entering the Roche lobe of the accretor larger than 10%. It quickly acquires angular momentum and within the shocked region, a disc-like structure is formed, whatever the cooling mechanism, with thicker discs for less efficient cooling. Because Vela X-1 is an eclipsing system and since we expect the wind-capture disc to form within the orbital plane, the thickness of the disc might significantly alter the absorbing column density : in the case of an inefficient cooling, the disc would be thick enough to intercept the line-of-sight and contribute to the observed absorbing column density. Also, Foulkes et al. (2010) showed that the precession of a disc wrapped by a radiative pressure driven instability (Pettersson and A. 1977a,b) could be responsible for the off-states observed in some systems, although mechanisms not relying on the presence of a disc have been proposed for Vela X-1 (see e.g. Manousakis and Walter 2015).
- the line-driven wind acceleration is more efficient than the one computed for a 1D steady atmosphere in Sander, Fürst, Kretschmar, Oskina, Todt, Hainich, Shenar and Hamann (2017), either because of a significant influence of the departure from a purely radial wind or because of a peculiar chemical composition of the donor star XXX ANDREAS : DO YOU KNOW HOW SENSITIVE YOUR RESULTS ARE ON THE CHEMICAL COMPOSITION YOU ASSUME? DID YOU TRY YOUR CODE ON A METAL RICH AND POOR STAR (ALTHOUGH I GUESS THE LINE-DRIVEN ACCELERATION IS NOT A MONOTONOUS FUNCTION OF THE METALLICITY)? XXX. In this case, the LF configuration, where the wind speed is slightly larger than the orbital speed, would be more representative of the wind accretion process at stake in Vela X-1 and no disc structure can form, whatever the cooling mechanism. The mass accretion rate, of the order of a few 0.1% of the stellar mass loss rate, would be consistent with the observed mean X-ray luminosity for typical values of η (i.e. ~ 5 to 10%).

The present study addressed the permanent behavior of the flow, but winds of massive stars are unstable and form internal shocks which lead to overdense clumps of matter (Owocki and Rybicki 1984; Sundqvist et al. 2017). The impact of these clumps on the time variability of the mass accretion rate has been investigated in El Mellah et al. (2017) but a wind fast enough to not be bent by the orbital effects was considered. The present work shows that, provided some systems display winds of velocity similar to the orbital speed, the orbital bending and the associated net angular momentum can not be neglected. Because the clumps carry themselves a local angular momentum, El Mellah et al. (2017) showed that clumpy wind accretion was less efficient than its homogeneous counterpart : including the microstructure of the wind might thus help to decrease the mass accretion rate at a few NS magnetosphere radii, but the influence of the clumps on the properties of the wind-capture disc (e.g. its permanence) remain to be studied. With a proper treatment of the effective viscosity in the disc and of the coupling between the disc and the magnetosphere, we could produce a physically-motivated synthetic curve of the torque applied to the NS as a function of time, opening the door to a consistent way to address the question of the NS spinning-up and down.

Acknowledgements. IEM wishes to thank Antonios Manousakis for fruitful discussions about the underlying computational aspects and the members of the X-wind collaboration for the observational consequences of the present analysis. IEM also thanks Wenbin Liu for the insightful discussions on the accretion of angular momentum. IEM has received funding from the Research Foundation Flanders (FWO) and the European Union's Horizon 2020 research and innovation program under the Marie Skłodowska-Curie grant agreement No 665501. IEM and JOS are grateful for the hospitality of the International Space Science Institute (ISSI), Bern, Switzerland which sponsored a team meeting initiating a tighter collaboration between massive stars wind and X-ray binaries communities. The simulations were conducted on the Tier-1 VSC (Flemish Supercomputer Center funded by Hercules foundation and Flemish government).

References

- Abbott, B. P., Abbott, R., Abbott, T. D. and Al, E. (2016), *Phys. Rev. Lett.* **116**(24), 241103.
- Armas Padilla, M., Degenaar, N. and Wijnands, R. (2013), *Mon. Not. R. Astron. Soc.* **434**(2), 1586–1592.
- Bachetti, M., Harrison, F. A., Walton, D. J., Grefenstette, B. W., Chakrabarty, D., Fürst, F., Barret, D., Beloborodov, A., Boggs, S. E., Christensen, F. E., Craig, W. W., Fabian, A. C., Hailey, C. J., Hornschemeier, A., Kaspi, V., Kulkarni, S. R., Maccarone, T., Miller, J. M., Rana, V., Stern, D., Tendulkar, S. P., Tomsick, J. I., Webb, N. A. and Zhang, W. W. (2014), *Nature*, Vol. 514, Issue 7521, pp. 202–204 (2014). **514**, 202–204.
- Blandford, R. D. and Begelman, M. C. (1999), *Mon. Not. R. Astron. Soc.* **303**(1), 1–5.
- Blondin, J. M., Kallman, T. R., Fryxell, B. A. and Taam, R. E. (1990), *Astrophys. J.* **356**, 591–608.
- Blondin, J. M. and Raymer, E. (2012), *Astrophys. J.* **752**(1), 30.
- Bozzo, E., Falanga, M. and Stella, L. (2008), *Astrophys. J.* **683**(2), 1031–1044.
- Castor, J. I., Abbott, D. C. and Klein, R. I. (1975), *Astrophys. J.* **195**, 157.
- Christians, J. (2012), *Int. J. Mech. Eng. Educ.* **40**(1), 53–65.
- Degenaar, N., Pinto, C., Miller, J. M., Wijnands, R., Altamirano, D., Paerels, F., Fabian, A. C. and Chakrabarty, D. (2017), *Mon. Not. R. Astron. Soc.* **464**(1), 398–409.
- Duchêne, G. and Kraus, A. (2013), *Annu. Rev. Astron. Astrophys.* **51**(1), 269–310.
- Edgar, R. G. (2004), *New Astron. Rev.* **48**(10), 843–859.
- El Mellah, I. and Casse, F. (2015), *Mon. Not. R. Astron. Soc.* **454**(3), 2657–2667.
- El Mellah, I. and Casse, F. (2016), *Mon. Not. R. Astron. Soc.* **467**(3), 2585–2593.
- El Mellah, I., Sundqvist, J. O. and Keppens, R. (2017), *MNRAS*.
- Foglizzo, T., Galletti, P. and Ruffert, M. (2005), *Astron. Astrophys.* **2201**(2001), 15.
- Foglizzo, T. and Ruffert, M. (1996), *Astron. Astrophys.* **361**, 22.
- Forman, W., Jones, C., Tananbaum, H., Gursky, H., Kellogg, E. and Giacconi, R. (1973), *Astrophys. J.* **182**, L103.
- Foulkes, S. B., Haswell, C. a. and Murray, J. R. (2010), *arXiv.org* **401**(2), 1275–1289.
- Frank, J., King, A. and Raine, D. J. (1986), *Phys. Today* **39**, 124.
- Fürst, F., Kreykenbohm, I., Pottschmidt, K., Wilms, J., Hanke, M., Rothschild, R. E., Kretschmar, P., Schulz, N. S., Huenemoerder, D. P., Klochkov, D. and Staubert, R. (2010), *Astron. Astrophys.* **519**, A37.
- Fürst, F., Pottschmidt, K., Wilms, J., Tomsick, J. A., Bachetti, M., Boggs, S. E., Christensen, F. E., Craig, W. W., Grefenstette, B. W., Hailey, C. J., Harrison, F., Madsen, K. K., Miller, J. M., Stern, D., Walton, D. J. and Zhang, W. (2014), *Astrophys. J.* **780**(2).
- Fürst, F., Walton, D. J., Harrison, F. A., Stern, D., Barret, D., Brightman, M., Fabian, A. C., Grefenstette, B., Madsen, K. K., Middleton, M. J., Miller, J. M., Pottschmidt, K., Ptak, A., Rana, V. and Webb, N. (2016), *Astrophys. J.* **831**(2), L14.
- Ghosh, P. and Lamb, F. K. (1978), *Astrophys. J.* **223**, L83.
- Ghosh, P. and Lamb, F. K. (1979), *Astrophys. J.* **234**, 296.
- Gimenez-Garcia, A., Shenar, T., Torrejon, J. M., Oskinova, L., Martinez-Nunez, S., Hamann, W.-R., Rodes-Roca, J. J., Gonzalez-Galan, A., Alonso-Santiago, J., Gonzalez-Fernandez, C., Bernabeu, G. and Sander, A. (2016), *Astron. Astrophys.* **591**(A26), 25.
- Gräfener, G., Koesterke, L. and Hamann, W.-R. (2002), *Astron. Astrophys.* **387**(1), 244–257.
- Grinberg, V., Hell, N., El Mellah, I., Neilsen, J., Sander, A. A. C., Leutenegger, M., Fürst, F., Huenemoerder, D. P., Kretschmar, P., Kühnel, M., Martínez-Núñez, S., Niu, S., Pottschmidt, K., Schulz, N. S., Wilms, J. and Nowak, M. A. (2017), *Astron. Astrophys. Vol. 608, id.A143*, 18 pp. **608**.
- Grinberg, V., Pottschmidt, K., Böck, M., Schmid, C., Nowak, M. A., Uttley, P., Tomsick, J. A., Rodriguez, J., Hell, N., Markowitz, A., Bodaghee, A., Bel, M. C., Rothschild, R. E. and Wilms, J. (2014), *arXiv.org*.
- Hamann, W.-R. and Koesterke, L. (1998), *Astron. Astrophys* **335**, 1003–1008.
- Hatchett, S. and McCray, R. (1977), *Astrophys. J.* **211**, 552.
- Hiltner, W. A., Werner, J. and Osmer, P. (1972), *Astrophys. J.* **175**, L19.
- Ho, C. and Arons, J. (1987), *Astrophys. J.* **316**, 283.
- Horedt, G. P. (2000), *Astrophys. J.* **541**(2), 821–830.
- Hu, C.-P., Chou, Y., Ng, C. Y., Lin, L. C.-C. and Yen, D. C.-C. (2017), *Astrophys. Journal*, Vol. 844, Issue 1, Artic. id. 16, 10 pp. (2017). **844**.
- Illarionov, A. F. and Sunyaev, R. A. (1975), *Astron. Astrophys.* **39**.
- Israel, G. L., Belfiore, A., Stella, L., Esposito, P., Casella, P., De Luca, A., Marelli, M., Papitto, A., Perri, M., Puccetti, S., Castillo, G. A. R., Salvetti, D., Tiengo, A., Zampieri, L., D’Agostino, D., Greiner, J., Haberl, F., Novara, G., Salvaterra, R., Turolla, R., Watson, M., Wilms, J., Wolter, A., Rodríguez Castillo, G. A., Salvetti, D., Tiengo, A., Zampieri, L., D’Agostino, D., Greiner, J., Haberl, F., Novara, G., Salvaterra, R., Turolla, R., Watson, M., Wilms, J. and Wolter, A. (2017), *Science* (80-.). **355**(6327), 817–819.
- Karino, S. (2014), *Publ. Astron. Soc. Japan* **66**(2), 2–3.
- Lin, D. N. C. and Papaloizou, J. C. B. (1985), *Protostars planets II (A86-12626 03-90)*. Tucson, AZ, Univ. Arizona Press. 1985, p. 981–1072. NSF-supported Res. p. 1293.
- Lucy, L. B. and Solomon, P. M. (1970), *Astrophys. J.* **159**, 879.
- MacLeod, M. and Ramirez-Ruiz, E. (2014).
- Manousakis, A. and Walter, R. (2015), *Astron. Astrophys.* **58**, A58.
- Manousakis, a., Walter, R. and Blondin, J. (2013).
- Martínez-Núñez, S., Kretschmar, P., Bozzo, E., Oskinova, L. M., Puls, J., Sidoli, L., Sundqvist, J. O., Blay, P., Falanga, M., Fürst, F., Gimenez-García, A., Kreykenbohm, I., Kühnel, M., Sander, A., Torrejón, J. M. and Wilms, J. (2017), *Space Sci. Rev.* **212**(1-2), 59–150.
- Medvedev, M. V. and Narayan, R. (2000), *Astrophys. Journal*, Vol. 554, Issue 2, pp. 1255–1267. **554**(2), 1255–1267.
- Mohamed, S. and Podsiadlowski, P. (2007).
- Motch, C., Pakull, M., Grisé, F. and Soria, R. (2011), *Astron. Nachrichten* **332**(4), 367–370.
- Narayan, R., Mahadevan, R. and Quataert, E. (1998), *Theory Black Hole Accretion Disk. - Cambridge Univ. Press* (1998), 36.
- Orosz, J. A., McClintock, J. E., Aufdenberg, J. P., Remillard, R. A., Reid, M. J., Narayan, R. and Gou, L. (2011), *Astrophys. J.* **742**(2), 84.
- Owocki, S. P. and Rybicki, G. B. (1984), *Astrophys. J.* **284**, 337.
- Paczynski, B. (1977), *Astrophys. J.* **216**, 822.
- Peterson, J. A. and A., J. (1977a), *Astrophys. J.* **214**, 550–559.
- Peterson, J. A. and A., J. (1977b), *Astrophys. J.* **216**(1), 827–837.
- Quaintrell, H., Norton, A. J., Ash, T. D. C., Roche, P., Willems, B., Bedding, T. R., Baldry, I. K. and Fender, R. P. (2003), *Astron. Astrophys.* **401**(1), 313–323.
- Rawls, M. L., Orosz, J. A., McClintock, J. E., Torres, M. A. P., Bailyn, C. D. and Buxton, M. M. (2011), *Astrophys. Journal*, Vol. 730, Issue 1, Artic. id. 25, 11 pp. (2011). **730**.
- Romano, P., Bozzo, E., Mangano, V., Esposito, P., Israel, G., Tiengo, A., Campana, S., Ducci, L., Ferrigno, C. and Kennea, J. A. (2015), *Astron. Astrophys.* **576**, 5–9.
- Saladino, M. I., Pols, O. R., van der Helm, E., Pelupessy, I. and Zwart, S. P. (2018), *eprint arXiv:1805.03208*.
- Sander, A. A. C., Fürst, F., Kretschmar, P., Oskinova, L. M., Todt, H., Hainich, R., Shenar, T. and Hamann, W.-R. (2017), *Astron. Astrophys.* **610**, A60.
- Sander, A. A. C., Hamann, W.-R., Todt, H., Hainich, R. and Shenar, T. (2017), *Astron. Astrophys. Vol. 603, id.A86*, 14 pp. **603**.
- Schure, K. M., Kosenko, D., Kaastra, J. S., Keppens, R. and Vink, J. (2009), *Astron. Astrophys. Vol. 508, Issue 2, 2009, pp.751-757* **757**, 751–757.
- Shakura, N. I., Postnov, K. A., Kochetkova, A. Y. and Hjalmarsdotter, L. (2013), *Physics-Uspokhi* **56**, 321–346.
- Shakura, N., Postnov, K., Kochetkova, A. and Hjalmarsdotter, L. (2012), *Mon. Not. R. Astron. Soc.* **420**(1), 216–236.
- Shapiro, S. L. and Lightman, A. P. (1976), *Astrophys. J.* **204**(10), 555.
- Smith, D. M., Heindl, W. A. and Swank, J. H. (2001), *Astrophys. Journal*, Vol. 569, Issue 1, pp. 362–380. **569**, 362–380.
- Sundqvist, J. O., Owocki, S. P. and Puls, J. (2017), *eprint arXiv:1710.07780*.
- Taam, R. E., Qiao, E., Liu, B. F. and Meyer-Hofmeister, E. (2018), *Astrophys. Journal*, Vol. 860, Issue 2, Artic. id. 166, 5 pp. (2018). **860**, 1–13.
- Toro, E. F., Spruce, M. and Speares, W. (1994), *Shock Waves* **4**(1), 25–34.
- Turner, N. J. and Stone, J. M. (2001), *Astrophys. J. Suppl. Ser.* **135**(1), 30.
- van Marle, A. J. and Keppens, R. (2011), *Comput. Fluids* **42**(1), 44–53.
- Vink, J. S., de Koter, A. and Lamers, H. J. G. L. M. (2001), *Astron. Astrophys. v.369, p.574-588* **369**, 61–64.
- Vreugdenhil, C. B. and Koren, B. (1993), Vieweg.
- Xia, C., Teunissen, J., Mellah, I. E., Chané, E. and Keppens, R. (2018), *Astrophys. J. Suppl. Ser.* **234**(2), 30.
- Ziolkowski, J. (1985), *Acta Astron. (ISSN 0001-5237)*, vol. 35, no. 3-4, 1985, p. 185–198. **35**(c), 1–4.